cells

MDPI

Article

Vagal Cholinergic Anti-Inflammatory Pathway and Gastrointestinal Microenvironment Remodeling Mediate Electroacupuncture Restoration of Gastric Motility in Functional Dyspepsia

Yiwen Tang, Weijie Tao, Huilin Chen, Bing Zhu and Shuya Wang *

Institute of Acupuncture and Moxibustion, China Academy of Chinese Medical Sciences, Beijing 100700, China; tangyiwen0315@163.com (Y.T.); tao_weijie@163.com (W.T.); hayleyhuilin@163.com (H.C.); zhubing@mail.cintcm.ac.cn (B.Z.)

* Correspondence: wangshuya@mail.cintcm.ac.cn

Abstract

Functional dyspepsia (FD) is closely associated with gastric dysmotility and enteric nervous system (ENS) dysfunction. Here, we investigated the mechanisms by which electroacupuncture (EA) at ST36 modulates in vivo ENS dynamics and restores gastric motility in FD. Using iodoacetamide-induced FD and *ChAT*^{GCaMP6s} transgenic mice, gastrointestinal (GI) transit was tracked via in vivo X-ray imaging, while the real-time calcium activity of antral myenteric cholinergic neurons was recorded through a customized optical gastric window. Concurrently, gastroduodenal tissue cytokines, brain–gut peptides, and motility-related proteins were systematically quantified. Our results demonstrated that EA significantly accelerated delayed gastric emptying and whole-gut transit. In vivo imaging revealed that EA reversed the pathological functional inertia of antral choline acetyltransferase-positive (ChAT+) neurons, elevating their activation rate from 1.11% in FD to 27.78%. Rather than replenishing depleted prokinetic hormones, EA selectively suppressed elevated inhibitory peptides (SST, CCK, VIP) to release the pathological "motor brake". Concurrently, EA intervention was associated with upregulated α7nAChR expression, attenuation of tissue proinflammatory cytokine levels, restored C-Kit protein expression, and downregulation of TRPV1 expression. These findings indicate that EA at ST36 rescues FD gastric dysmotility by awakening dormant cholinergic motor neurons and releasing the inhibitory neuroendocrine brake via coordinated neuro-immune regulation.

Keywords: functional dyspepsia; electroacupuncture; myenteric plexus; cholinergic anti-inflammatory pathway; calcium imaging; neuro-immune interaction

Check for updates

Academic Editor: Jiande Chen

Received: 23 September 2026
Revised: 26 October 2026
Accepted: 11 November 2026
Published: 18 November 2026

Copyright: © 2026 by the authors. Licensee MDPI, Basel, Switzerland. This article is an open access article distributed under the terms and conditions of the Creative Commons Attribution (CC BY) license.

1. Introduction

Functional dyspepsia (FD) is a highly prevalent functional gastrointestinal (GI) disorder characterized by gastric dysmotility, upper digestive tract low-grade mucosal microinflammation, and visceral hypersensitivity [1,2]. Impaired gastric motility and delayed antral emptying form the primary pathophysiological basis for postprandial fullness and early satiety [3]. Concurrently, localized proinflammatory cytokine accumulation initiates and maintains mucosal microenvironmental dysfunction [4,5], while peripheral sensory afferent sensitization abnormally amplifies visceral nociceptive signaling to induce hyperalgesic symptoms such as epigastric burning and pain [6]. Although these multidimensional abnormalities are clinically well documented, the underlying cellular and neurobiological mechanisms driving their coordinated dysregulation remain incompletely understood.

Acupuncture at Zusanli (ST36) represents an effective non-pharmacological therapy with established clinical and experimental evidence for alleviating GI dysmotility [7,8]. Neurobiological studies indicate that the ST36 region is richly innervated by prokineticin receptor 2 (PROKR2)-positive deep fascial sensory fibers [9–11]. Electroacupuncture (EA) at appropriate intensities transmits somatic sensory inputs via the spinal cord to the nucleus tractus solitarius and the dorsal motor nucleus of the vagus (DMV) in the brainstem. This central activation subsequently drives vagal parasympathetic efferent projections to abdominal target organs, thereby accelerating gastric emptying and coordinating GI motor rhythms.

The enteric nervous system (ENS) serves as the intrinsic neural network that independently and precisely governs smooth muscle contraction and propulsive motility [12,13]. Within the myenteric plexus, choline acetyltransferase-positive (ChAT+) neurons represent the primary excitatory motor subtype, whose release of acetylcholine (ACh) provides the fundamental cellular drive for smooth muscle contraction [14–16]. Coordinated gastric motility also depends closely on interstitial cells of Cajal (ICCs), the pacemakers for GI electrical slow waves [17]. The varicosities of ChAT+ cholinergic neurons reside in close proximity to the ICC network to establish functional coupling. While ICCs generate the basal slow-wave rhythm, excitatory transmitters released by ChAT+ neurons modulate slow-wave depolarization amplitude and trigger smooth muscle action potentials [18], together forming the core functional unit for antral electromechanical coupling.

Under FD pathology, however, multiple localized microenvironmental abnormalities severely impair the functional state of cholinergic neurons. Chronic exposure to elevated local proinflammatory cytokines destabilizes the membrane potential of enteric neurons and blunts their firing responsiveness [5,19]. Meanwhile, the depletion of prokinetic peptides (motilin, gastrin, and ghrelin) combined with the aberrant accumulation of inhibitory peptides (SST, CCK, and VIP) imposes a persistent neuroendocrine "brake" [20–23]. Furthermore, compensatory upregulation of the transient receptor potential vanilloid 1 (TRPV1) channel mediates prominent pain sensitization [6,24,25]. Along with the suppressed expression of the ICC pacemaker marker C-Kit, these factors synergistically drive gastric antral ChAT+ neurons into profound "pathological functional inertia" [23,26].

To address these questions, this study utilized an in vivo gastric window combined with a single-photon calcium imaging system in $ChAT^{GCaMP6s}$ transgenic mice [7,27]. We integrated continuous in vivo X-ray tracking of GI transit [28,29], multiplex electrochemiluminescence assays for cytokine profiling [30], and targeted Western blot assays [23,31]. Through these approaches, we captured the real-time spiking of gastric antral cholinergic neurons induced by EA at ST36 in FD mice. Furthermore, we systematically dissected how EA restores gastric motility by releasing the inhibitory peptide brake, activating the vagal cholinergic anti-inflammatory pathway (CAP), repairing the ICC pacemaker network, and suppressing TRPV1-mediated hyperalgesia. Collectively, these findings provide solid cellular electrophysiological and neuro-immunological evidence supporting the clinical application of acupuncture therapy for functional GI disorders.

2. Materials and Methods

2.1. Animals and Ethical Approval

Male C57BL/6J mice (8–10 weeks old, 25 ± 3 g) were used in this study. For in vivo calcium imaging, ChAT-IRES-Cre ($ChAT^{Cre}$) mice (JAX:006410, The Jackson Laboratory, Bar Harbor, ME, USA) were crossed with Rosa26-LSL-GCaMP6s ($Rosa26^{GCaMP6s}$) mice (JAX:028866, The Jackson Laboratory, ME, USA) to produce $ChAT^{GCaMP6s}$ mice that express GCaMP6s in cholinergic neurons (8–10 weeks old, 25 ± 3 g). All mice were housed in an SPF animal room at 22 ± 1 °C and 55 ± 5% humidity under a 12 h light/dark cycle. Mice

were kept at up to five per cage, with free access to standard food and water. Mice were anesthetized with isoflurane (2–3% for induction, 1–1.5% for maintenance; R510-22-10, RWD Life Science, Shenzhen, China) during surgery and imaging.

All animal procedures followed the Guiding Opinions on the Treatment of Experimental Animals from the Ministry of Science and Technology of China and were approved by the Committee on the Ethics of Animal Experiments at the China Academy of Chinese Medical Sciences (approval no. D2024-01-26-07).

2.2. Adeno-Associated Virus (AAV) Microinjection in Gastric Antrum

All surgeries were performed under aseptic conditions. Mice were anesthetized with isoflurane (2–3% for induction and 1–1.5% for maintenance) on a heating pad. The stomach was accessed through an anterior median incision, and a sterilized swab was used to move the liver upwards to expose the full extent of the gastric antrum. rAAV9-CAG-GCaMP6s (2.00×10^{12} vg/mL, BrainVTA Co., Ltd., Wuhan, China) virus was injected at five different loci (200 nL per point and 100 nL/min) into the muscle layer of the gastric antrum by using a microsyringe (Microliter Syringe: 5 µL, 7633-01; Small Hub Removable Needle: 34 gauge, 207434-07; Hamilton Company, Shanghai, China). The needle was kept in place for 3–5 min after each injection to prevent leakage. After injection, the muscle layer of the abdominal incision was sutured once, and the skin was sutured to close the wound, which was then treated with iodophor. Meloxicam (0.2 mg/kg, Qilu Animal Health Products Co., Ltd., Jinan, China) was administered subcutaneously for postoperative analgesia and anti-inflammation. All mice injected with rAAV underwent a 28-day waiting period before window implantation to allow for full expression of the virus [27].

2.3. FD Model Induction and Body Weight Monitoring

To establish the FD mouse model, mice were gavaged with 0.1% iodoacetamide (IA) solution (0.1 mL/10 g of body weight) daily between 9:00 and 10:00 AM for 7 consecutive days. Mice in the control group received an equal volume of purified water [32,33].

Body weight was measured daily between 8:30 and 9:00 AM from Day 1 to Day 7 (modeling period) and from Day 8 to Day 10 (EA treatment period). Normalized body weight was calculated as follows: relative body weight = (body weight on Day n/body weight on Day 1) [34].

2.4. EA in Mice

The mice were anesthetized with isoflurane (1–1.5%), and their body temperature was maintained at 35.5–37.5 °C. ST36 was located approximately 4 mm below the knee joint and 2 mm lateral to the anterior tibial tubercle. For bilateral EA stimulation, paired stainless-steel needles (0.16 × 7 mm, separated by 1 mm) were inserted perpendicularly into the tibialis anterior muscle to a depth of 3–4 mm [7]. Stimulation was delivered at 1.5 mA and 15 Hz using Han's Acupoint Nerve Stimulator (HANS-200A, Jason Scientific, Nanjing, China).

For the gastric emptying experiment, control mice received a single 15 min EA stimulation to evaluate acute gastric emptying. For therapeutic intervention in FD mice, animals received four 15 min EA sessions across 3 consecutive days. The first session was delivered on the afternoon of Day 7, followed by once-daily sessions at a fixed time from Day 8 to Day 10. For in vivo calcium imaging, mice received a 120 s EA stimulation during each recording period.

2.5. In Vivo Gastric Window Implantation and Calcium Imaging

2.5.1. Gastric Window Implantation

The mice were anesthetized with isoflurane (1–1.5%), and their stomach was exposed through an abdominal incision. As described in a previous study [27], a custom-made gastric window was inserted into the incision and secured to the abdominal wall using a purse-string suture [35] to minimize respiratory motion artifacts. A gastric scaffold was placed through the window and guided underneath the gastric antrum to provide stable support without tissue compression. The coverslip and circlip were then mounted into the window groove to seal the chamber.

2.5.2. In Vivo Calcium Imaging Recording

To prevent muscle twitching and ensure adequate anesthetic depth, mice underwent a tracheotomy for tracheal intubation and were connected to a mechanical ventilator (SomnoSuite, Kent Scientific, Torrington, CT, USA) delivering 0.5% isoflurane intratracheally. In vivo calcium imaging of GCaMP6s-expressing myenteric neurons in the gastric antrum was performed using a Leica single-photon imaging system (STELLARIS 8, Leica Microsystems, Shanghai, China). Mice in the control group were recorded continuously for 180 s without further intervention. For the EA group and FD + EA group, mice were recorded for a 30 s baseline (Pre), followed by 120 s of EA stimulation at ST36 (1.5 mA, 15 Hz) and a 30 s post-stimulation period (Post).

Fluorescence image sequences were collected continuously throughout the 180 s period (Figure S1A).

2.5.3. Calcium Imaging Data Analysis

The NoRMCorre package was used to correct motion artifacts and enhance the signal-to-noise ratio [36]. Processed image stacks were imported into MATLAB (R2022a) for quantitative analysis using a custom MATLAB script (Proca). Individual neuronal regions of interest (ROIs) were manually selected to extract frame-by-frame mean gray values. The relative fluorescence change was defined as $\Delta F/F_0 = (F - F_0)/F_0$, where F represents the fluorescence intensity during the stimulation period (0–120 s) and F_0 represents the average baseline fluorescence during the 10 s before stimulation (−10 to 0 s). Neurons with a mean $\Delta F/F_0 \geq 20\%$ during the stimulation period were defined as activated [7].

2.6. GI Motility Recording

2.6.1. In Vivo X-Ray Assessment of GI Motility

Mice were fasted for 8 h with free access to water and then orally gavaged with 0.5 mL of a 50% (w/v) barium sulfate suspension. Following gavage, abdominal X-ray images were collected at 0, 30, 60, and 90 min using a Carestream in vivo multispectral imaging system (Fx Pro, Carestream Health, Rochester, NY, USA) [28,29].

In acute experiments, the first X-ray image was acquired immediately after barium meal gavage, before acute EA (15 min) or anesthesia. In FD modeling and EA intervention experiments, images were captured immediately after 7 days of model induction (Day 0, Pre), to confirm delayed gastric emptying, and immediately after completing four EA sessions over 3 days (Day 3, Post) to assess therapeutic efficacy. ROIs for the stomach and intestine were delineated using Carestream analysis software to measure gastric X-ray transmission intensity, residual barium area, and intestinal transit distance. Normalized to the baseline values at 0 min, the dynamic change in gastric transmission intensity (Intensity, %), residual gastric barium area (Area, %), and GI propulsion rate (Propulsion, %) were calculated

across all time points. To evaluate the therapeutic effect of EA, the difference between post- and pre-treatment values (Δ = Post − Pre) was calculated for comparisons between groups.

2.6.2. Liquid Meal Gastric Emptying Assay

Following the experimental intervention period, mice were fasted with free access to water for 8 h. Each mouse was orally gavaged with a calibrated volume of liquid nutrient meal (0.5 mL per mouse), and the exact mass of the administered meal (W_{meal}) was recorded. At 20 min post-gavage, mice were promptly euthanized by cervical dislocation, and a laparotomy was performed. The stomach was ligated at both the cardia and pylorus to prevent luminal content leakage and carefully excised. Surface moisture was blotted dry with filter paper, and the total weight of the intact stomach with luminal contents (W_{full}) was weighed. The stomach was subsequently opened along the greater curvature, thoroughly rinsed with ice-cold 1× PBS (Servicebio, Wuhan, China) to remove residual contents, blotted dry, and weighed empty (W_{empty}). The gastric emptying rate was calculated using the following equation:

$$\text{Gastric Emptying Rate } (\%) = [1 - (W_{full} - W_{empty})/W_{meal}] \times 100\%$$

2.7. Tissue Harvesting

Following the completion of EA intervention or parallel anesthesia, mice were euthanized by cervical dislocation for tissue collection. After isolation, the stomach was opened along the greater curvature and thoroughly washed with 4 °C 1× PBS to remove luminal contents. A 1.5 cm duodenal segment immediately distal to the pylorus was excised, opened longitudinally, and rinsed with 4 °C 1× PBS. Tissue specimens were placed into 2.0 mL cryogenic vials (430488, Corning, Shanghai, China), snap-frozen in liquid nitrogen, and stored at −80 °C for subsequent ELISA, multiplex electrochemiluminescence assays, and Western blot assays.

2.8. Enzyme-Linked Immunosorbent Assay (ELISA)

Levels of GI hormones and brain–gut peptides, including motilin, gastrin, ghrelin, vasoactive intestinal peptide (VIP), somatostatin (SST), and cholecystokinin (CCK), were measured in gastric and duodenal tissues using commercial ELISA kits (Motilin: CEA575Mu; Gastrin: CEB224Mu; Ghrelin: CEA991Mu; VIP: CEA380Mu; SST: SEA592Mu; CCK: CEA802Mu; Cloud-Clone Corp., Wuhan, China). Tissue homogenates were centrifuged at 12,000× *g* for 15 min at 4 °C to collect the supernatants, and assays were performed in strict accordance with the manufacturers' instructions. Optical density (OD) was measured at 450 nm using a microplate reader. Concentrations were calculated from standard curves, normalized to total protein concentrations determined by the BCA method, and expressed as pg/mg of total protein.

2.9. Multiplex Electrochemiluminescence Assay

Gastric and duodenal tissues were homogenized in lysis buffer containing protease and phosphatase inhibitors. Total protein concentration was determined using a BCA protein assay kit (abs9232, Absin, Shanghai, China). Cytokine levels (including IFN-γ, IL-1β, IL-2, IL-4, IL-6, IL-10, IL-12p70, IL-5, KC/GRO and TNF-α) were measured using a multiplex electrochemiluminescence kit (LXMM10-1, LabEx, Shanghai, China) on a MESO QuickPlex (MSD-SQ120, Meso Scale Diagnostics, Rockville, MD, USA) reader in strict accordance with the manufacturer's instructions. Concentrations of each cytokine were calculated from the standard curves, normalized to the total protein content of each sample, and expressed as pg/mL of total protein.

2.10. Western Blot Assay

Frozen gastric and duodenal tissues were homogenized in RIPA lysis buffer containing protease and phosphatase inhibitors. The lysates were centrifuged at 12,000× *g* for 15 min at 4 °C, and the supernatants were collected. Total protein concentration was determined using a BCA protein assay kit (abs9232, Absin, Shanghai, China).

Equal amounts of protein were separated on 8–12% SDS-PAGE gels according to molecular weight and transferred onto PVDF membranes. Membranes were blocked with 5% non-fat milk (Servicebio, Wuhan, China) in TBST for 1 h at room temperature and incubated overnight at 4 °C on a shaker with the following antibodies: rabbit polyclonal anti-α7nAChR antibody (1:1000, ab216485, Abcam, Cambridge, UK; 54 kDa); rabbit monoclonal anti-c-Kit antibody (1:2000, ab256345, Abcam; 145 kDa); rabbit monoclonal anti-nNOS (neuronal) antibody (1:1000, ab76067, Abcam; 161 kDa); mouse monoclonal anti-TRPV1 antibody (1:1000, ab203103, Abcam; 95 kDa). Mouse monoclonal anti-GAPDH (1:20,000, YM3029, ImmunoWay, San Jose, CA, USA; 37 kDa) was used as an internal loading control.

The next day, membranes were washed three times with TBST (5 min each) and incubated with HRP-conjugated goat anti-rabbit or goat anti-mouse IgG secondary antibodies (1:5000) for 1 h at room temperature. Protein bands were visualized using an enhanced chemiluminescence kit (Absin, Shanghai, China) and captured using a chemiluminescence imaging system. Band intensities were quantified with ImageJ (version 1.54p, National Institutes of Health, Bethesda, MD, USA) and normalized to GAPDH.

2.11. Statistical Analysis

All data were statistically analyzed and graphed using GraphPad Prism 10.0 (GraphPad Software, San Diego, CA, USA). Data are presented as mean ± standard error of the mean (mean ± SEM).

Before parametric statistical inference, data normality was evaluated using the Shapiro–Wilk test (or Kolmogorov–Smirnov test), and homogeneity of variance was assessed using the Brown–Forsythe test. Statistical methods were selected based on data distribution:

Two-group comparisons (Figure S1F): For normally distributed data with equal variance, an unpaired two-tailed Student's *t*-test was used. For normally distributed data with unequal variance, Welch's *t*-test was applied. For non-normally distributed data, the non-parametric Mann–Whitney *U* test was performed.

Multiple-group comparisons (Figures 5B,C, 6A,B, 7A,B and Figure S1E): Differences among three or more groups were evaluated by ordinary one-way analysis of variance (ANOVA) followed by Tukey's or Dunnett's post hoc test for normally distributed data with equal variance. If variances were unequal, Welch's ANOVA followed by Dunnett's T3 post hoc test was used. For skewed (non-normally distributed) data, the non-parametric Kruskal–Wallis test followed by Dunn's post hoc test was conducted.

Hierarchical/nested analysis for in vivo calcium imaging (Figures 2F–I, 4I,J and Figure S2A–L): To account for the hierarchical structure of calcium imaging data (multiple neurons recorded within individual mice, $n = 90$ neurons nested within $N = 5$ mice per group) and avoid pseudoreplication, linear mixed-effects models were applied, treating individual mouse identity as a random nested factor. Specifically, a nested two-tailed *t*-test was used for two-group comparisons (Figure 2H,I) and a nested one-way ANOVA followed by Tukey's multiple comparisons test was used for four-group comparisons (Figure 4I,J and Figure S2A–L). Furthermore, for longitudinal time-course calcium dynamics (Figures 2F,G and 4G,H) and animal-level responder rates (Figure S1F,G), values were first averaged or calculated per mouse ($N = 5$ mice/group) as the independent biological replicate before performing two-way RM ANOVA, an unpaired Student's *t*-test, or one-way ANOVA across animals.

Time-course dynamic measurements (Figure 1C–E, Figure 2F,G, Figure 3C–E and Figure S1D): Longitudinal comparisons across consecutive time points or time windows were performed using two-way repeated-measures (RM) ANOVA or a mixed-effects model (to accommodate missing values), followed by Šídák's post hoc test for multiple comparisons at individual time points.

Overall dynamic effect evaluation (Figure 3C–E, Figure 4G,H and Figure S1D): To evaluate cumulative differences across the observation period, the area under the curve (AUC) was calculated for each animal or neuron. The resulting AUC values were then compared among groups using ordinary one-way ANOVA (for equal variance) or the Kruskal–Wallis test (for non-normally distributed data).

All statistical tests were two-tailed, and differences were considered statistically significant at $p < 0.05$. Significance levels are denoted as follows: * $p < 0.05$, ** $p < 0.01$, *** $p < 0.001$, **** $p < 0.0001$; # $p < 0.05$, ## $p < 0.01$, ### $p < 0.001$, #### $p < 0.0001$.

3. Results

3.1. Acute EA at ST36 Enhances Gastric Emptying and GI Motility Under Physiological Conditions

To evaluate the impact of EA at ST36 on GI motility under physiological conditions, healthy mice were subjected to real-time, continuous in vivo X-ray imaging for 0–90 min following the oral administration of a 50% (w/v) barium sulfate suspension (Figure 1A). Representative pseudocolor X-ray images revealed that a single 15 min EA stimulation (1.5 mA, 15 Hz) accelerated gastric emptying of the barium meal and facilitated barium transit into the distal intestine compared with the parallel-anesthetized control (Ctrl) group (Figure 1B).

Quantitative analysis demonstrated that the percentage change in gastric X-ray transmission intensity (Intensity, %) was significantly elevated in the EA group at 60 and 90 min post-gavage compared with the Ctrl group (Figure 1C; $p < 0.01$ at 60 min, $p < 0.0001$ at 90 min; overall effect: $p < 0.0001$). Correspondingly, the normalized residual gastric barium area (Area, %) in the EA group exhibited a rapid decline at both 60 and 90 min (Figure 1D; $p < 0.01$ and $p < 0.001$, respectively; overall effect: $p < 0.001$), further confirming that EA substantially enhances gastric clearance. Furthermore, EA significantly enhanced the intestinal propulsion rate (Propulsion, %), as evidenced by the extended migration distance of the barium front at 90 min (Figure 1E; $p < 0.001$; overall effect: # $p < 0.05$). Collectively, these findings indicate that acute EA stimulation at ST36 substantially promotes gastric emptying and propulsive GI motility under physiological states.

3.2. Real-Time In Vivo Calcium Imaging Reveals That EA at ST36 Activates Gastric Myenteric Neurons

Given that the myenteric plexus within the ENS directly orchestrates GI smooth muscle contractility, we subsequently investigated whether an EA-induced prokinetic effect resulted from the direct excitation of local myenteric neurons. To test this, rAAV9-CAG-GCaMP6s was microinjected in situ into the gastric antrum of the mice. Following a 28-day viral expression period, a customized gastric window was secured, allowing for real-time in vivo calcium imaging via a single-photon microscope (Figure 2A,B and Figure S1A). The fluorescence recording protocol lasted 180 s, including a 30 s baseline period (Pre), a 120 s EA stimulation period (EA), and a 30 s post-stimulation period (Post). Heatmaps of the single-neuron calcium responses revealed that the majority of the myenteric neurons in the control (Ctrl) group remained quiescent during recording, exhibiting a negligible spontaneous activation rate of only 2.22% (2/90) (Figure 2C,D, top). Conversely, acute EA stimulation rapidly triggered robust calcium transients across a vast neuronal population upon onset, significantly expanding the proportion of activated neurons to 41.11% (37/90)

(Figure 2C,D, bottom) and significantly increasing the neuronal responder rate per mouse ($p < 0.01$ vs. Ctrl; Figure S1F). Dynamic calcium traces indicated that the mean fluorescence intensity ($\Delta F/F_0$) of these myenteric neurons rose rapidly upon EA stimulation, sustained an elevated plateau throughout the stimulation period, and gradually returned to baseline post-stimulation (Figure 2E).

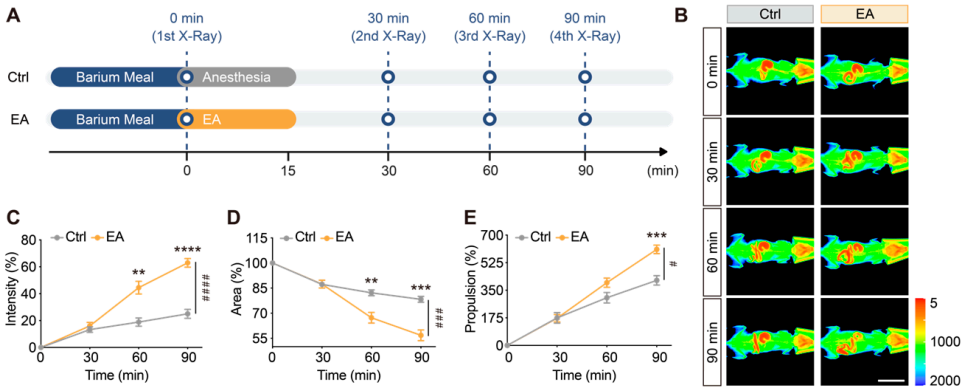


Figure 1. EA at ST36 promotes gastric emptying and motility in mice. (**A**) Experimental protocol for X-ray imaging. (**B**) Representative pseudocolor X-ray images of the Ctrl and EA groups from 0 to 90 min (color bar: 5–2000; scale bar: 3 cm). Quantitative analysis of the dynamic change rate of gastric X-ray intensity (**C**), normalized residual gastric barium area (**D**), and intestinal propulsion rate (**E**) in the Ctrl and EA groups from 0 to 90 min. Data are expressed as mean ± SEM ($N = 10$ mice/group). # $p < 0.05$, ### $p < 0.001$, #### $p < 0.0001$ vs. Ctrl for overall effect; ** $p < 0.01$, *** $p < 0.001$, **** $p < 0.0001$ vs. Ctrl at individual time points.

Time-binned quantitative analysis at the animal level demonstrated that both the mean and peak fluorescence intensity (Mean and Peak $\Delta F/F_0$) of myenteric neurons in the EA group were significantly higher than those in the Ctrl group across all stimulation intervals (0–30 s, 30–60 s, 60–90 s, and 90–120 s) (Figure 2F,G; $p < 0.0001$). Hierarchical nested analysis of neuronal profiles across the entire recording further confirmed that both global mean $\Delta F/F_0$ and peak $\Delta F/F_0$ were significantly elevated by EA (Figure 2H, $p < 0.01$; Figure 2I, $p < 0.05$). Representative calcium imaging fields (Figure 2J) and the corresponding spatiotemporal heatmaps (Figure 2K) visually illustrated the synchronized activation of local circuits during EA. Single-neuron trace analysis of 20 representative cells within this field highlighted that EA onset (0 s) triggered prominent calcium spikes followed by sustained oscillations in most cells, which reliably returned to baseline after stimulation offset (120 s) (Figure S1B). Collectively, these data substantiate that EA at ST36 directly excites gastric antral myenteric neurons in vivo via peripheral neural pathways.

3.3. EA at ST36 Reverses Gastric Dysmotility and Restores GI Transit in a Mouse Model of FD

To establish the non-organic FD model, mice received a daily gavage of 0.1% IA solution (iodoacetamide; Sigma-Aldrich, St. Louis, MO, USA) for 7 consecutive days. Subsequently, the modeled mice underwent four sessions of EA at ST36 over 3 days (FD + EA group) or were exposed to parallel anesthesia alone (FD group) (Figure 3A). Radiographic quantification revealed severe impairments in GI motility within the FD group compared to healthy controls (Ctrl), characterized by delayed gastric clearance and restricted intestinal transit (Figure 3B). By calculating the longitudinal parameter shifts (Δ = Post − Pre), we observed that the untreated FD group exhibited sustained motility deficits without spontaneous recovery, as indicated by gastric transmission intensity (ΔIntensity), residual gastric barium area (ΔArea), and intestinal transit values (ΔPropulsion) hovering around or below baseline levels (Figure 3B–E).

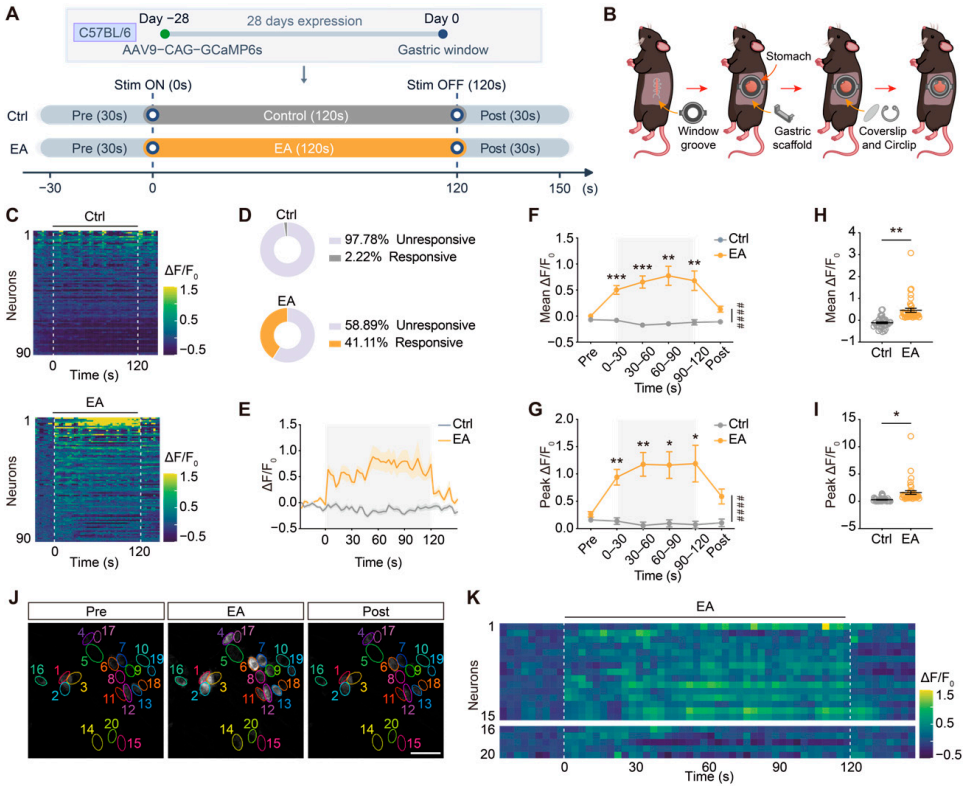


Figure 2. EA at ST36 modulates gastric ENS neuronal activity in mice. (**A**) Experimental design and timeline for in vivo gastric ENS neuronal calcium imaging (Pre: 30 s, Stimulation: 120 s, Post: 30 s). (**B**) Schematic diagram of the surgical steps for gastric window implantation. (**C**) Heatmaps showing single-neuron calcium responses in the Ctrl and EA groups (n = 90 neurons/group; dashed lines: stimulation ON and OFF; color bar: $\Delta F/F_0$, −0.5–1.5). (**D**) Proportion of responsive neurons in each group. (**E**) Dynamic calcium signaling response curves of myenteric plexus neurons. (**F**) Quantitative comparison of the mean $\Delta F/F_0$ and (**G**) peak $\Delta F/F_0$ across different time points between two groups (gray shading represents the stimulation period). (**H**) Quantitative comparison of the mean $\Delta F/F_0$ and (**I**) peak $\Delta F/F_0$ of individual neurons during the recording period. (**J**) Representative calcium fluorescence ENS images of neurons (#1–#20) at the Pre, EA, and Post stages (scale bar: 50 μm). (**K**) Dynamic $\Delta F/F_0$ heatmap of 20 representative neurons shown in (**J**). Data are expressed as mean ± SEM (N = 5 mice/group, n = 90 neurons/group). #### $p < 0.0001$ vs. Ctrl for overall effect; * $p < 0.05$, ** $p < 0.01$, *** $p < 0.001$ vs. Ctrl at individual time points.

Remarkably, EA intervention at ST36 effectively counteracted these impairments. In the FD + EA group, ΔIntensity steadily increased from 30 to 90 min, showing the greatest recovery at 90 min (Figure 3C; $p < 0.0001$ vs. FD), while ΔArea clearance was substantially accelerated in the FD + EA group, with values at 60 and 90 min significantly lower than those in both Ctrl and FD groups (Figure 3D; $p < 0.0001$ vs. FD; overall intergroup comparison: $p < 0.0001$ vs. Ctrl and FD). Meanwhile, EA treatment restored impaired whole-gut transit (ΔPropulsion). Transit speed accelerated starting from 30 min, performing significantly better than the FD group (Figure 3E; $p < 0.001$). Starting from 60 min, the rate of increase in transit was also significantly higher than that in the Ctrl group (Figure 3E; $p < 0.0001$).

Histopathological examination confirmed that the mucosal architecture of both the gastric antrum and duodenum remained intact and well organized across all groups, ruling out organic lesions (Figure S1C). Body weight monitoring and conventional liquid meal assays further validated that EA successfully mitigated the FD-induced systemic wasting phenotype and accelerated delayed gastric emptying (Figure S1D,E). Together, these histopathological findings, general physical signs, liquid meal emptying results, and in vivo

dynamic X-ray imaging demonstrate that EA at ST36 reverses non-organic delayed gastric emptying and restores coordinated GI transit in the FD model.

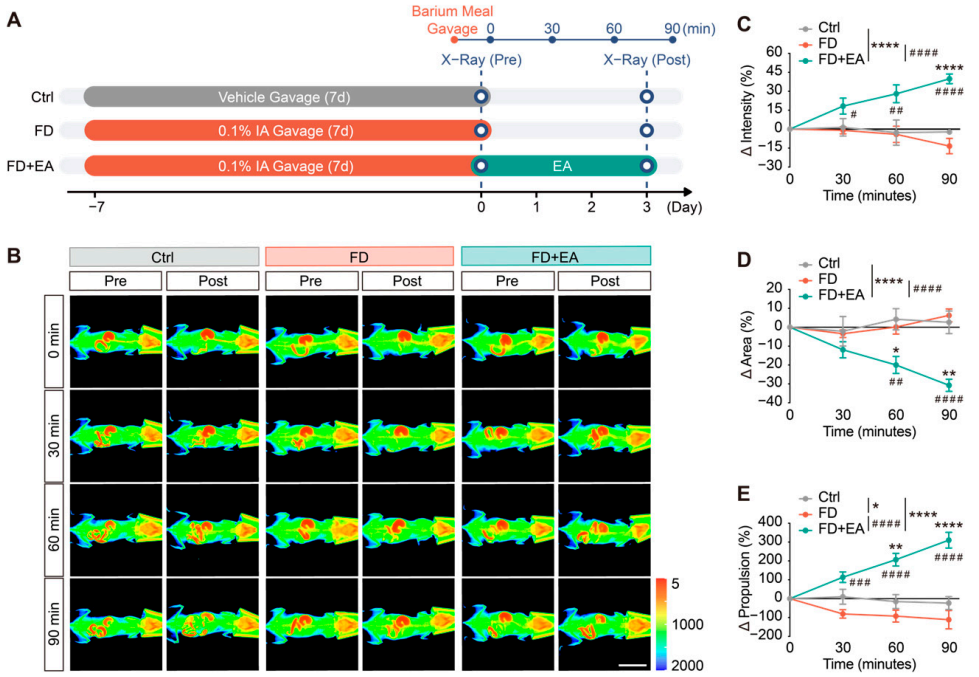


Figure 3. EA at ST36 improves gastric emptying and GI motility disorders in FD mice. (**A**) Experimental timeline and workflow for X-ray imaging across the Ctrl, FD, and FD + EA groups. (**B**) Representative pseudocolor X-ray images of barium transit from 0 to 90 min (color bar: 5–2000; scale bar: 3 cm). Differences before and after intervention (Δ = Post − Pre) in gastric X-ray intensity change percentage (**C**), normalized residual gastric barium area (**D**), and GI propulsion rate (**E**) among the three groups from 0 to 90 min. Data are expressed as mean ± SEM (n = 6–10 mice/group). * $p < 0.05$, ** $p < 0.01$, **** $p < 0.0001$ vs. Ctrl; # $p < 0.05$, ## $p < 0.01$, ### $p < 0.001$, #### $p < 0.0001$ vs. FD.

3.4. EA Rejuvenates Suppressed Spontaneous Activity and Dynamic Fluctuation of Gastric Cholinergic Neurons Under FD Pathology

Cholinergic neurons (ChAT+) represent the primary excitatory motor neurons within the ENS that orchestrate smooth muscle contractility and GI motility. To elucidate the cellular mechanism underlying EA-mediated motility recovery in FD, we crossed $ChAT^{Cre}$ mice with $Rosa26^{GCaMP6s}$ (Ai96) mice to achieve lineage-specific expression of GCaMP6s in cholinergic motor neurons ($ChAT^{GCaMP6s}$ mice). We monitored real-time in vivo calcium signals in gastric myenteric cholinergic neurons across four groups: Ctrl, Ctrl + EA, FD, and FD + EA (Figure 4A). Single-neuron heatmap and activation rate analyses revealed that 11.11% (10/90) of cholinergic neurons in the Ctrl group exhibited spontaneous baseline activity (Figure 4B). Acute EA stimulation (Ctrl + EA) significantly increased this responsive fraction to 22.22% (20/90) (Figure 4C). Conversely, cholinergic neurons in untreated FD mice manifested marked functional suppression, with the activation rate plunging to a negligible 1.11% (1/90) (Figure 4D). Remarkably, EA intervention in FD mice (FD + EA) successfully re-engaged these hyporesponsive neurons, restoring the overall activation rate to 27.78% (25/90) (Figure 4E). Consistent with the pooled neuronal proportions, animal-level quantification of responder rates per mouse confirmed that EA significantly elevated the percentage of responsive cholinergic neurons in both healthy ($p < 0.05$, Ctrl + EA vs. Ctrl) and FD mice ($p < 0.01$, FD + EA vs. FD; Figure S1G).

Dynamic fluorescence traces and time-binned averages revealed distinct calcium response kinetics across groups. In control mice, baseline spontaneous calcium activity during the pre-stimulation baseline period (Pre) was minimal in both the Ctrl and Ctrl + EA groups (Figure S2A,G). However, acute EA at ST36 abruptly evoked robust and sustained calcium transients in cholinergic neurons (Ctrl + EA; Figure 4C,F). Across all stimulation intervals (0–30 s, 30–60 s, 60–90 s, and 90–120 s), both the Mean and Peak $\Delta F/F_0$ in the Ctrl + EA group were significantly elevated compared with the Ctrl group (Figure 4G,H, $p < 0.0001$; Figure S2B–E, $p < 0.0001$; Figure S2H–K, $p < 0.001$ or $p < 0.0001$). This state of heightened excitation partially persisted into the post-stimulation recovery phase (Figure S2F, $p < 0.0001$; Figure S2L, $p < 0.001$).

Compared with the Ctrl group, cholinergic neurons in untreated FD mice exhibited no significant alteration in peak $\Delta F/F_0$ across most observation windows. Intriguingly, during the 30–60 s period, the mean $\Delta F/F_0$ in the FD group appeared paradoxically higher than that in the Ctrl group (Figure S2C; $p < 0.01$). Spatiotemporal heatmap analysis resolved this paradox: healthy Ctrl neurons underwent continuous, low-amplitude physiological fluctuations encompassing both spontaneous firing and transient downward baseline fluorescence fluctuations at rest, which mathematically yielded a minor negative baseline shift. Conversely, FD pathology severely extinguished these basal oscillatory dynamics, locking the enteric circuits into a rigid, non-responsive quiescent state lacking any physiological fluctuations. These observations indicate that FD pathology induces a profound loss of dynamic signaling range and basal calcium responsiveness in cholinergic motor neurons.

Crucially, EA intervention effectively rescued this pathological quiescence in FD mice (Figure 4E,F), successfully recruiting and rejuvenating the hyporesponsive cholinergic neurons. Throughout the EA period, both the mean and peak $\Delta F/F_0$ values in the FD + EA group were robustly restored (Figure 4G,H; $p < 0.0001$). Time-binned single-neuron analysis confirmed that baseline activity (Pre) was uniformly suppressed across all experimental groups (Figure S2A,G). Upon EA onset (0–30 s), neurons in the FD + EA group exhibited an immediate surge in both mean and peak $\Delta F/F_0$ compared with the FD group (Figure S2B,H; $p < 0.0001$ vs. FD). This heightened activity remained significantly elevated during the 30–60 s interval for both mean (Figure S2C; $p < 0.01$) and peak $\Delta F/F_0$ (Figure S2I; $p < 0.05$) and persisted into the 60–90 s window for mean $\Delta F/F_0$ (Figure S2D; $p < 0.05$) before gradually tapering during the late stimulation window (90–120 s; Figure S2E,K) and returning to baseline after stimulation offset (Figure S2F,L).

Hierarchical nested analysis across the entire recording session further confirmed these intergroup differences (Figure 4I,J). Overall mean and peak $\Delta F/F_0$ were significantly elevated in the Ctrl + EA group relative to the Ctrl group (Mean $\Delta F/F_0$: $p < 0.0001$; Peak $\Delta F/F_0$: $p < 0.001$). While neurons in the FD group showed no overall statistical difference in mean or peak $\Delta F/F_0$ compared to the Ctrl group, EA treatment in the FD + EA group produced a marked restoration of acute calcium responsiveness compared to the FD group (mean $\Delta F/F_0$: $p < 0.001$; peak $\Delta F/F_0$: $p < 0.01$).

Representative in situ imaging fields (Figure 4K,M) and corresponding dynamic heatmaps (Figure 4L,N) directly illustrated the activation patterns of local cholinergic neurons. Real-time tracking of 20 representative neurons per field highlighted that EA onset (0 s) evoked prominent calcium spikes and sustained fluorescence in normally quiescent neurons (#1–#9) under physiological conditions (Figure 4L). Under FD pathology, EA successfully disrupted the network-wide silence, awakening and synchronously recruiting dormant cholinergic motor neurons (#1–#11; Figure 4N).

Collectively, these findings indicate that EA at ST36 serves as a potent excitatory driver to activate gastric cholinergic pathways under physiological conditions. Under FD pathology, EA successfully overcomes disease-induced functional inertia, thereby acutely

restoring the neural excitability and dynamic signaling range of enteric cholinergic motor circuits.

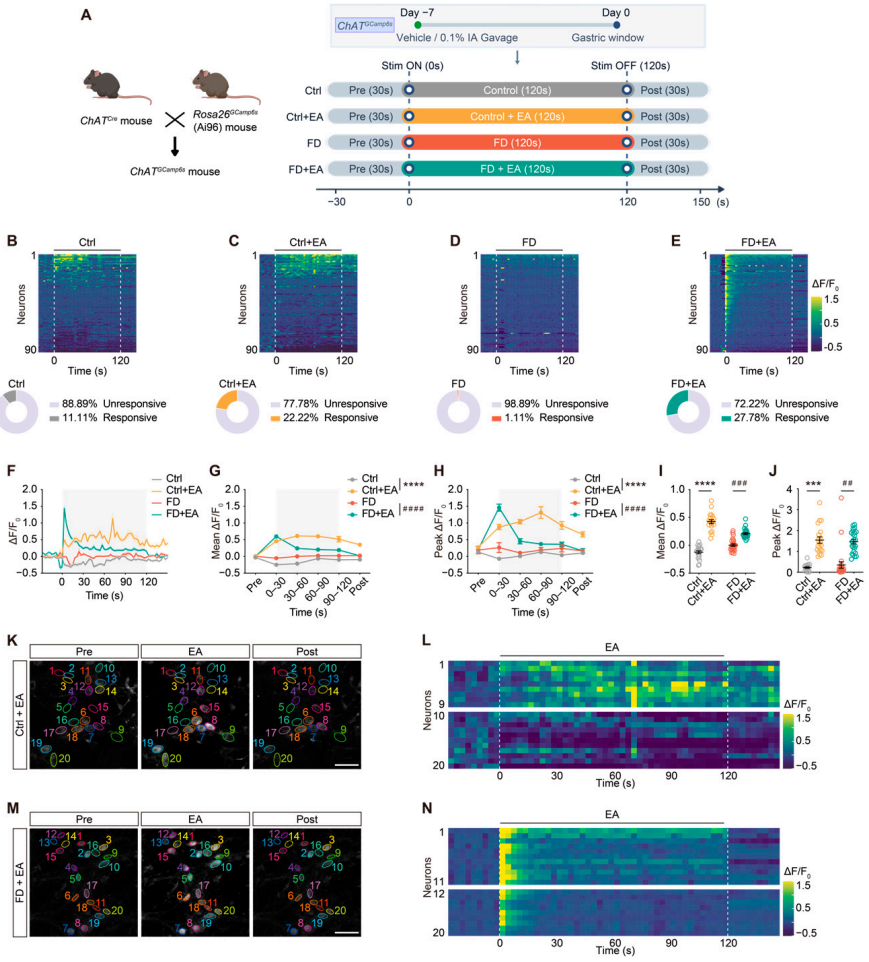


Figure 4. EA at ST36 activates gastric cholinergic neuronal activity in FD mice. (**A**) Genetic breeding strategy for generating *ChAT*^{GCaMP6s} mice and experimental timeline for in vivo gastric cholinergic calcium imaging. (**B**–**E**) Heatmaps of single-neuron calcium responses (n = 90 neurons/group; dashed lines: stimulation ON and OFF; color bar: $\Delta F/F_0$, −0.5–1.5) and the respective proportion of responsive neurons in different groups. (**F**) Dynamic calcium signaling response curves of myenteric plexus neurons. (**G**) Quantitative comparison of the mean $\Delta F/F_0$ and (**H**) Peak $\Delta F/F_0$ across different time intervals (gray shading: stimulation period). Quantitative comparison of the mean $\Delta F/F_0$ (**I**) and peak $\Delta F/F_0$ (**J**) of individual neurons during the recording period. (**K**) Representative calcium images of neurons (#1–#20) in the Ctrl + EA group during Pre, EA, and Post stages, where neurons #1–#9 are activated (scale bar: 50 μm). (**L**) Dynamic $\Delta F/F_0$ heatmap of 20 representative neurons shown in (**K**). (**M**) Representative calcium images of neurons #1–#20 in the FD + EA group during Pre, EA, and Post stages, where neurons #1–#11 are activated (scale bar: 50 μm). (**N**) Dynamic $\Delta F/F_0$ heatmap of 20 representative neurons shown in (**M**). Data are expressed as mean ± SEM (N = 5 mice/group, n = 90 neurons/group). *** $p < 0.001$, **** $p < 0.0001$ vs. Ctrl; ## $p < 0.01$, ### $p < 0.001$, #### $p < 0.0001$ vs. FD.

3.5. EA at ST36 Remodels the GI Neuroendocrine Profile and Suppresses Tissue Microinflammation in FD Mice

To elucidate the neuroendocrine–immune network modulating EA-mediated motility recovery, gastric antral and duodenal tissues were harvested following a 3-day EA regimen for downstream ELISA, multiplex electrochemiluminescence assays, and Western blot assays (Figure 5A).

Multiplex GI hormone profiling demonstrated that FD induction disrupted the homeostatic balance between prokinetic and inhibitory peptides (Figure 5B,C). Intrigued by the persistent reduction in prokinetic elements (motilin, gastrin, and ghrelin) post-stimulation, these data imply that EA does not restore GI motility via the direct replenishment of prokinetic hormones. Instead, EA potently downregulates inhibitory peptides—specifically VIP, CCK, and SST—thereby lifting the pathological "brake" on GI transit and re-establishing neuroendocrine homeostasis.

Concurrently, electrochemiluminescence-based cytokine signature mapping revealed that FD mice manifested a characteristic low-grade microinflammation in the upper GI tract (Figure 6A,B). Crucially, EA treatment extensively dampened this proinflammatory cascade by suppressing the aberrant accumulation of IFN-γ, IL-1β, IL-2, IL-5, and IL-12p70 in the gastric antrum. In the duodenum, FD induction triggered a pronounced inflammatory shift characterized by pathological elevation of the proinflammatory cytokine IL-12p70 ($p < 0.05$) and a marked downregulation of the anti-inflammatory mediator IL-10 ($p < 0.01$) compared with the Ctrl group. Crucially, EA intervention extensively remodeled this local tissue immune microenvironment. It robustly suppressed the local proinflammatory cascade, as evidenced by a substantial reduction in duodenal IL-1β, IL-6, IL-5, and IL-12p70 levels ($p < 0.01$ vs. FD). Intriguingly, while EA effectively extinguished the active inflammatory cascade, it did not fully reset the basal immune homeostasis; gastric KC/GRO and duodenal IL-10 levels in the FD + EA group remained comparable to those in untreated FD mice. Notably, EA stimulation also drove several duodenal cytokines (IL-1β, IL-6, and IL-5) significantly below Ctrl baselines ($p < 0.05$), highlighting a potent, multitargeted suppressive effect on local tissue microinflammation. This potent anti-inflammatory action effectively eliminates the neuro-destructive impact of local immune stress on myenteric networks, thereby providing a permissive microenvironment for the functional restoration of enteric motor circuits.

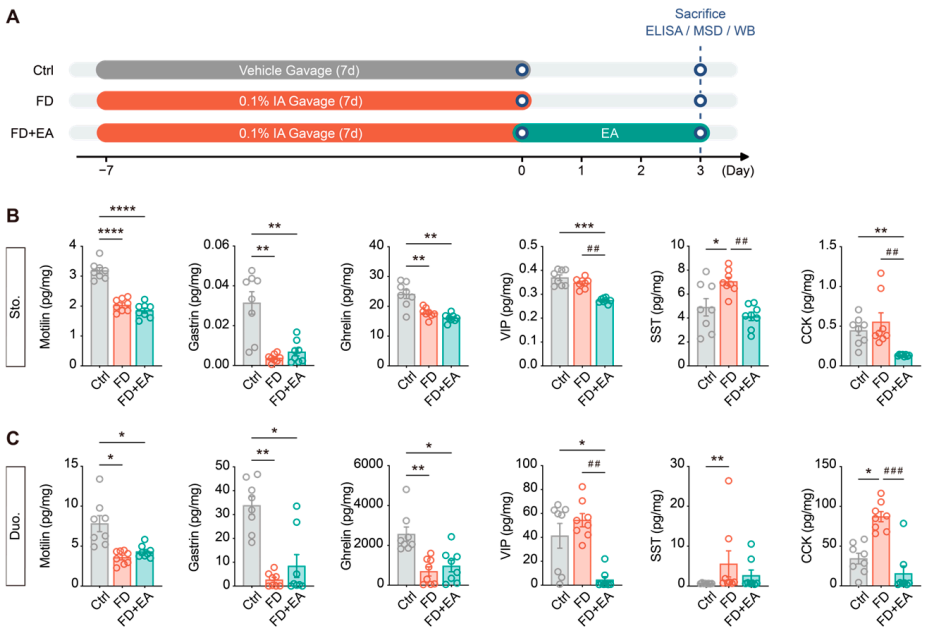


Figure 5. EA at ST36 balances brain–gut peptides in FD mice. (**A**) Experimental timeline for animal modeling, EA intervention and tissue collection. (**B**,**C**) Expression levels of brain–gut peptides and GI hormones, including motilin, gastrin, ghrelin, VIP, SST, and CCK (pg/mg) in gastric (**B**) and duodenal (**C**) tissues. Data are expressed as mean ± SEM ($n = 8$ mice/group). * $p < 0.05$, ** $p < 0.01$, *** $p < 0.001$, **** $p < 0.0001$ vs. Ctrl; ## $p < 0.01$, ### $p < 0.001$ vs. FD.

3.6. EA at ST36 Modulates Motility-Related Protein Expression in the Gastric Antrum of FD Mice

To elucidate the downstream molecular targets through which EA promotes gastric emptying and reactivates cholinergic neurons, Western blot assays were performed on gastric antrum tissues. We specifically evaluated key proteins involved in neuromuscular motility, pacemaker function (ICCs), and visceral sensation, with protein expression levels normalized to GAPDH (Figure 7A,B).

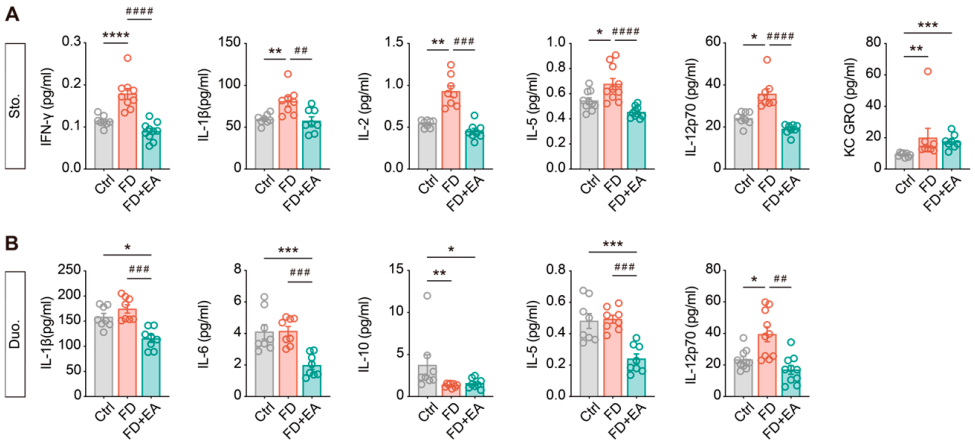


Figure 6. EA at ST36 alleviates the tissue microinflammatory profile in the gastric antrum and duodenum of FD mice. (**A**) Quantitative comparison of proinflammatory cytokines and chemokines in mouse gastric antral tissues (Sto.) measured by multiplex electrochemiluminescence assays, including IFN-γ, IL-1β, IL-2, IL-5, IL-12p70, and KC/GRO. (**B**) Quantitative comparison of cytokine levels in mouse duodenal tissues (Duo.), including proinflammatory cytokines (IL-1β, IL-6, IL-5, and IL-12p70) and the anti-inflammatory cytokine IL-10. Data are expressed as mean ± SEM (N = 8–10 mice/group). * $p < 0.05$, ** $p < 0.01$, *** $p < 0.001$, **** $p < 0.0001$ vs. Ctrl; ## $p < 0.01$, ### $p < 0.001$, #### $p < 0.0001$ vs. FD.

Representative bands and densitometric analysis revealed that several critical proteins were significantly downregulated in the FD group compared with healthy controls (Ctrl). These included α7nAChR (a key receptor in the CAP; $p < 0.05$), C-Kit (a marker for ICCs; $p < 0.01$), and nNOS (an enzyme synthesizing inhibitory neurotransmitters; $p < 0.01$). Meanwhile, the protein expression of TRPV1, an ion channel closely linked to visceral hypersensitivity, was markedly upregulated ($p < 0.01$). Notably, EA treatment at ST36 (FD + EA group) effectively reversed this pathological imbalance in the gastric antrum. Specifically, EA intervention significantly restored the suppressed protein levels of α7nAChR ($p < 0.05$ vs. FD) and C-Kit ($p < 0.01$ vs. FD), while robustly suppressing TRPV1 overexpression ($p < 0.001$ vs. FD) to a level even lower than that observed in the Ctrl group ($p < 0.05$ vs. Ctrl). In contrast, gastric nNOS expression exhibited no significant alterations following EA intervention compared with the untreated FD group.

These quantitative findings demonstrate that EA at ST36 specifically upregulates α7nAChR and C-Kit expression while suppressing TRPV1 hyperactivity within the gastric antrum. Integrated with our physiological and cellular findings, these results indicate that EA at ST36 corrects gut peptide imbalances and alleviates the constraints imposed by inhibitory hormones. Furthermore, EA upregulates α7nAChR protein levels alongside reduced local proinflammatory cytokines. By restoring C-Kit protein expression and downregulating the nociceptive marker TRPV1, EA comprehensively ameliorates gastric dysmotility in FD mice at systemic, cellular, and molecular levels. Consequently, these targets offer critical insights into the molecular translation of acupuncture and underscore its therapeutic potential for functional GI disorders.

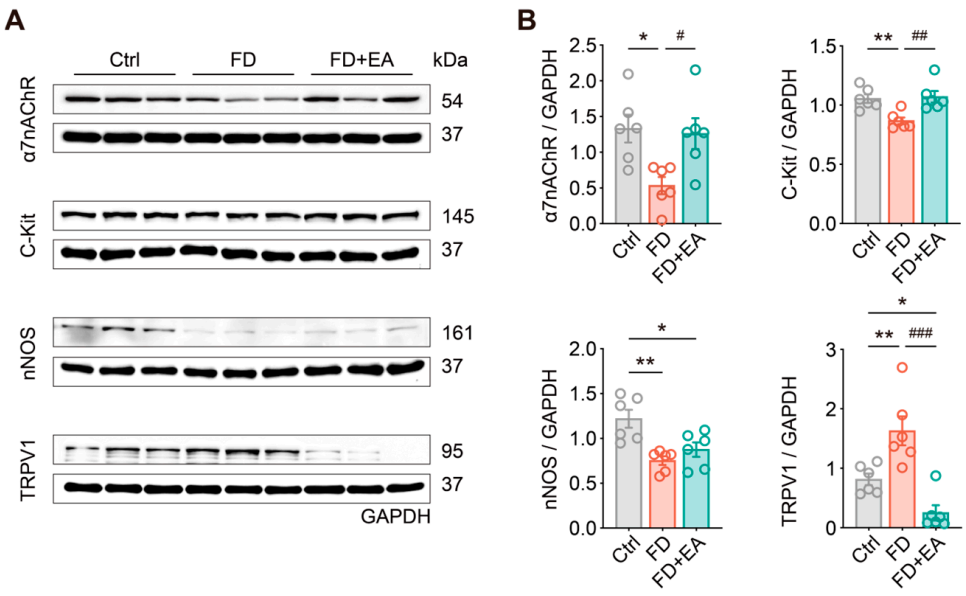


Figure 7. EA at ST36 modulates motility- and neuromodulation-related protein expression in the gastric antrum of FD mice. (**A**) Representative Western blot bands of α7nAChR, C-Kit, nNOS, and TRPV1 proteins in mouse gastric antral tissues (Sto.), with GAPDH as the internal loading control. (**B**) Densitometric quantification of α7nAChR, C-Kit, nNOS, and TRPV1 protein expression normalized to GAPDH across groups. Data are expressed as mean ± SEM ($n = 6$ mice per group). * $p < 0.05$, ** $p < 0.01$ vs. Ctrl; # $p < 0.05$, ## $p < 0.01$, ### $p < 0.001$ vs. FD.

4. Discussion

4.1. EA Reverses FD-Induced Functional Inertia of Gastric Cholinergic Neurons

As a core component of the ENS, the myenteric plexus directly governs the rhythmic contraction and propulsive motility of GI smooth muscle [12,13]. In this study, we combined a customized in vivo gastric window with a single-photon fluorescence imaging system. By employing *ChAT*^{GCaMP6s} transgenic mice to selectively label ChAT+ neurons, we achieved continuous, high-resolution, real-time recordings of gastric myenteric neural populations in living mice. Crucially, we captured a critical cellular hallmark in FD pathogenesis. In healthy control mice, cholinergic neurons at rest maintained dynamic physiological fluctuations, alternating between spontaneous calcium transients and quiescent baseline intervals, with a spontaneous activation rate of 11.11% [37]. Conversely, in iodoacetamide-induced FD mice, the proportion of responsive neurons dropped sharply to 1.11%. Their calcium traces exhibited a flatline pattern without physiological fluctuations, and the average fluorescence remained locked near baseline. This pattern indicates that gastric cholinergic neurons fell into profound pathological functional inertia [38,39]. This narrowed response range and functional silencing deprived the gastric antrum of sufficient excitatory drive. From a cellular electrophysiological perspective, these findings elucidate why FD mice experienced delayed emptying even in the absence of organic mucosal lesions such as ulcers or erosions [40].

Under this pathological state, acute EA at ST36 demonstrated a robust capacity to restore neural function. Previous studies have demonstrated that stimulating ST36 modulates GI motility via vagal parasympathetic reflexes [10,41]. In situ heatmaps and single-cell traces confirmed that EA immediately broke the electrical silence of the network upon onset. EA rapidly awakened dormant cholinergic motor neurons, restoring the activation rate to 27.78% and evoking high-amplitude, sustained calcium oscillations with significant increases in both Mean and Peak $\Delta F/F_0$ [7,14]. These findings indicate that EA at ST36 effectively overcomes disease-induced neuronal blunting during acute stimulation. It acutely

enhances the calcium excitability and responsiveness of the gastric cholinergic network, providing a direct cellular engine for smooth muscle contraction and luminal emptying.

4.2. Neuroendocrine Remodeling Releases the Inhibitory "Motor Brake" Rather than Forcing Prokinetic Output

GI hormones and brain–gut peptides form a microenvironmental network that regulates gut motility. Classic prokinetic peptides, including motilin, gastrin, and ghrelin, stimulate motility by directly activating smooth muscle or parasympathetic nerve terminals [20–22]. In contrast, SST, VIP, and CCK act as physiological "brakes" that relax gastric smooth muscle, delay gastric emptying, and induce fullness [20,23,40].

Conventional clinical therapies frequently rely on prokinetic receptor agonists to stimulate gastric emptying. However, direct receptor activation often triggers rapid receptor desensitization (tachyphylaxis) and severe adverse effects, such as cardiac arrhythmias and QTc prolongation. These safety concerns restrict their long-term clinical utility [2,21,42]. In the current study, profiling of peptides in the gastric antrum and duodenum revealed that FD mice exhibited a marked depletion of motilin, gastrin, and ghrelin, alongside the pathological accumulation of SST and CCK [23,40]. Notably, following EA at ST36, depleted motilin, gastrin, and ghrelin levels did not show an immediate rebound and remained relatively low. In sharp contrast, EA significantly reduced the abnormal accumulation of antral SST and duodenal CCK. In fact, certain inhibitory peptides, including tissue VIP and antral CCK, dropped even below healthy control baselines.

This selective regulation reveals a distinct mechanism by which EA restores neuroendocrine homeostasis. Under sustained pathological stress in FD, endogenous enteroendocrine cells suffer from functional exhaustion. Rather than forcing a rebound of prokinetic hormones, EA selectively targets and releases the pathological "motor brake" imposed by excessive VIP, CCK, and SST [37,43,44]. Releasing this inhibitory brake significantly lowers the resistance threshold for smooth muscle contraction. This relief enables reactivated cholinergic motor neurons to effectively drive propulsive gastric emptying.

4.3. Somatosensory–Autonomic Reflex and Microenvironmental Clearance Associated with the Gastric CAP

Recent reviews by Tian et al. (2025) [45] and Luo et al. (2026) [46] have systematically characterized the neuroanatomical basis of acupuncture, highlighting how the "acupoint-autonomic nerve–target organ immunity" axis enables multisystem, multitarget regulation. The ST36 region is richly innervated by deep fascia sensory afferents from PROKR2-positive sensory neurons. Appropriate EA stimulation ascends through the spinal cord to the nucleus tractus solitarius and the DMV in the brainstem. Vagal parasympathetic efferent pathways then precisely project neural impulses to abdominal target organs [9,10]. Specifically, the selection of the hindlimb ST36 acupoint and the stimulation parameters (1.5 mA, 15 Hz) in our protocol are grounded in this somatosensory–autonomic reflex specificity. Recent neuroanatomical studies demonstrate that low-to-moderate-intensity stimulation (such as 1.5 mA at 15 Hz) at ST36 selectively engages deep fascial PROKR2+ sensory fibers to activate the brainstem DMV–vagal efferent loop and enhance gastric motility, whereas high-intensity stimulation (>3 mA) cross-activates spinal sympathetic pathways that impede gastrointestinal transit [7,9,10]. Thus, our stimulation regimen operates within the optimal biophysical window required to selectively drive vagal prokinetic output without eliciting sympathetic inhibition.

Low-grade mucosal microinflammatory infiltration is widely recognized as a key factor that initiates and sustains FD [5,19]. In this study, multiplex electrochemiluminescence assays showed that FD mice developed marked low-grade microinflammation in the gastric

antrum and duodenum. This was characterized by the abnormal accumulation of IFN-γ, IL-1β, IL-2, IL-5, IL-12p70, and KC/GRO [47–50], alongside severe depletion in the anti-inflammatory cytokine IL-10 [50]. Prolonged local exposure to elevated inflammatory cytokines inevitably alters the neurophysiological, neurochemical, and morphological properties of the ENS [51,52].

Compelling evidence shows that acupuncture can alleviate systemic inflammation by modulating autonomic nerve activity [53,54]. EA at ST36 exhibited broad and potent anti-inflammatory effects, substantially clearing core proinflammatory cytokines in both the gastric antrum and duodenum. Western blot results further showed that gastric antral α7nAChR expression was significantly suppressed in FD mice and was markedly restored after EA intervention. Together, these findings provide strong correlative evidence supporting the involvement of the local CAP. Specifically, EA activates peripheral sensory nerves to drive vagal efferent activity, thereby promoting ACh release from myenteric cholinergic neurons in the gastric antrum. Previous studies indicate that released ACh can interact with α7nAChR expressed on local immune cells (such as resident macrophages) to inhibit proinflammatory transcription pathways and block cytokine production [55–58], which aligns with the concurrent whole-tissue α7nAChR upregulation and cytokine reduction observed in our homogenate assays. In addition, as shown by Zheng et al. (2021) [59], ACh can stimulate monocytic myeloid-derived suppressor cells (M-MDSCs) to synthesize and release IL-10 via the nAChR/ERK pathway, further reinforcing anti-inflammatory protection. Clearing this inflammatory toxicity creates a cleansed microenvironment, allowing cholinergic motor neurons to regain their normal electrophysiological activity.

4.4. Restoration of the Gastric Pacemaker Network and Modulation of Visceral Sensory Pathways

Coordinated gastric emptying relies on balanced cooperation between neural excitatory output, myoelectric slow-wave generation, and visceral afferent signals. By assessing regulatory proteins of motility and sensation in the gastric antrum, we further identified the molecular targets of EA.

ICCs initiate the slow-wave electrical rhythm in GI smooth muscle [60,61]. In FD mice, the expression of the pacemaker marker C-Kit decreased significantly in the gastric antrum, reflecting a loss in ICC-associated marker protein [26]. EA treatment effectively restored C-Kit protein levels, suggesting a recovery of the molecular substrate associated with gastric pacemaker activity, although direct morphological reconstruction of ICC networks remains to be histologically confirmed [23].

TRPV1 is a key channel mediating visceral noxious stimuli and hyperalgesia [6]. In the gastric antrum of FD mice, TRPV1 protein expression was significantly upregulated, reflecting a pathological state of sensory pain sensitization. This finding aligns with the common epigastric pain symptoms reported in FD patients [6,24,25]. EA at ST36 markedly suppressed this overexpression of TRPV1, reducing it to levels even below the normal baseline [31]. These results demonstrate that while promoting gastric motility, EA at ST36 markedly downregulates peripheral TRPV1 protein expression associated with visceral nociception, although direct behavioral assessments of visceral pain remain to be evaluated in future studies. Although gastric nNOS expression decreased significantly in FD mice, it showed no notable change after EA intervention. This indicates that the prokinetic action of EA in the gastric antrum specifically targets cholinergic excitatory circuits and ICC pacemaker networks rather than non-specific inhibitory pathways.

Clinically, these findings match the Rome IV criteria, which classify FD into postprandial distress syndrome (PDS, delayed emptying) and epigastric pain syndrome (EPS, gastric pain and hypersensitivity) [1,2]. By activating cholinergic neurons and restoring C-Kit expression, EA relieves the motor delay typical of PDS. Meanwhile, downregulating TRPV1

expression and reducing tissue cytokines target the molecular pathways associated with EPS. This dual effect highlights the practical value of EA at ST36 in treating both motor and sensory symptoms in FD.

4.5. Conclusions and Future Directions

While our findings provide compelling evidence for the therapeutic efficacy of EA, this study requires deeper investigation into the cell-specific and circuit-level mechanisms within the gastric microenvironment.

First, our current molecular and neuroendocrine profiling primarily relied on bulk assays, such as ELISA, multiplex electrochemiluminescence assays, and Western blot, using whole-thickness tissue homogenates from the gastric antrum and duodenum. While these tissue-level analyses successfully capture the macroscopic shift in the local microenvironment, they lack the resolution to distinguish cell-autonomous signaling from non-cell-autonomous adjustments within specific cellular subsets. Crucially, however, by demonstrating in vivo that gastric cholinergic ChAT+ neurons undergo profound pathological functional inertia during FD, our study establishes a foundational premise that renders single-cell resolution studies highly essential. Future research utilizing *ChAT*^{Cre}; *Ai14* fluorescent reporter mice, combined with fluorescence-activated cell sorting or single-cell RNA sequencing, will be able to map the precise cell-specific transcriptomic landscape and intracellular signaling cascades that govern this ChAT+ neuronal blunting and its subsequent rescue by EA.

Furthermore, while this investigation focused mainly on cholinergic excitatory motor neurons, other key cellular constituents, including nitrergic inhibitory neurons (nNOS+), VIP+ neurons, and enteric glial cells, also participate in the fine regulation of GI motor rhythms. Future work could apply subtype-specific chemogenetics (DREADDs) or optogenetics to selectively manipulate the cooperative networks among distinct enteric neuronal subsets and glial cells during EA-promoted gastric emptying.

Finally, while we verified changes in peripheral receptor expression and the immune microenvironment, the causal necessity of this anti-inflammatory pathway was not directly validated using loss-of-function manipulations (such as α7nAChR antagonism or vagotomy). Moreover, the full neuronal circuits from acupoint somatosensory afferents to autonomic afferents require more direct anatomical support. Future investigations employing trans-multisynaptic neurotropic viral tracing are needed to definitively trace the structural circuit connecting PROKR2-positive sensory afferents at the ST36 acupoint, the brainstem DMV, and local myenteric ChAT+ neurons. Systematically testing different stimulation parameters (such as frequency and intensity) and treatment durations will also help advance EA toward precise and controllable bioelectronic medicine.

Additionally, another methodological limitation of the present study is the absence of sham electroacupuncture (needling without electrical current) and off-target non-acupoint control groups. Although our anatomical rationale and stimulation parameter selection support the selective recruitment of ST36-associated deep fascial PROKR2+ afferents, future investigations will incorporate sham EA and non-acupoint stimulation to rigorously separate acupoint-specific autonomic regulation from generalized somatic sensory responses.

In summary, this study demonstrates that EA at ST36 drives a somatosensory–autonomic reflex to restore gastric motility through two complementary pathways. First, it suppresses the abnormal accumulation of inhibitory neuropeptides (VIP, CCK, and SST) to release the motor brake on gastric transit. Second, it is associated with upregulated gastric α7nAChR expression, reduced tissue proinflammatory cytokines, restored C-Kit protein levels, and downregulated TRPV1 expression. Together, these actions reverse the pathological functional inertia of gastric myenteric cholinergic neurons, acutely restore the

calcium responsiveness and dynamic range of local neural circuits, and ultimately rescue delayed gastric emptying and whole-gut transit dysfunction in FD mice.

Supplementary Materials: The following supporting information can be downloaded at https://www.mdpi.com/article/10.3390/cells15222106/s1: Figure S1: In vivo gastric imaging setup, neuronal calcium traces, phenotypic validation of FD mice, and animal-level neuronal responder rates, related to Figures 2–4. (A) Photograph of the in vivo calcium imaging setup for gastric antral neurons. Mice underwent tracheotomy and mechanical ventilation, and the gastric window was anchored beneath the 25× objective on a stabilization platform. (B) Dynamic calcium traces ($\Delta F/F_0$) of 20 representative gastric myenteric neurons from Figure 2J across the recording duration (dashed lines: stimulation ON and OFF at 0 s and 120 s). (C) Representative H&E staining images of gastric antrum (Sto.) and duodenum (Duo.) across groups (scale bar: 200 μm). (D) Dynamic curves of normalized body weight during the modeling (Days 1–7) and intervention (Days 8–10, yellow shading) periods (normalized to Day 1). (E) Gastric emptying rate (Emptying, %) 20 min after liquid nutrient meal gavage. (F) Percentage of responsive myenteric neurons per mouse in the Ctrl and EA groups ($N = 5$ mice/group), related to Figure 2D. (G) Percentage of responsive cholinergic neurons per mouse across the Ctrl, Ctrl + EA, FD, and FD + EA groups ($N = 5$ mice/group), related to Figure 4B–E. Data are expressed as mean ± SEM. * $p < 0.05$, ** $p < 0.01$, *** $p < 0.001$, **** $p < 0.0001$ vs. Ctrl; ## $p < 0.01$, ### $p < 0.001$, #### $p < 0.0001$ vs. FD; Figure S2: Scatter plots of mean and peak ΔF/F0 in gastric cholinergic neurons across time windows in *ChAT*^{GCaMP6s} mice, related to Figure 4. (A–F) Mean $\Delta F/F_0$ of individual cholinergic neurons during baseline (Pre, (A)), stimulation periods (0–30 s, (B); 30–60 s, (C); 60–90 s, (D); 90–120 s, (E)), and post-stimulation period (Post, (F)) in Ctrl, Ctrl + EA, FD, and FD + EA groups. Related to Figure 4G. (G–L) Peak ΔF/F0 of individual cholinergic neurons during baseline (Pre, (G)), stimulation periods (0–30 s, (H); 30–60 s, (I); 60–90 s, (J); 90–120 s, (K)), and post-stimulation period (Post, (L)) in each group. Related to Figure 4H. Data are expressed as mean ± SEM ($N = 5$ mice/group, $n = 90$ neurons/group) and analyzed using nested one-way ANOVA. ** $p < 0.01$, *** $p < 0.001$, **** $p < 0.0001$ vs. Ctrl; # $p < 0.05$, ## $p < 0.01$, #### $p < 0.0001$ vs. FD.

Author Contributions: Conceptualization, Y.T. and S.W.; methodology, Y.T. and S.W.; validation, Y.T.; formal analysis, Y.T. and W.T.; investigation, Y.T., W.T. and H.C.; data curation, Y.T. and W.T.; writing—original draft, Y.T.; writing—review and editing, Y.T. and S.W.; visualization, B.Z. and S.W.; supervision, B.Z. and S.W.; funding acquisition, B.Z. and S.W. All authors have read and agreed to the published version of the manuscript.

Funding: This study was funded by the Scientific and Technological Innovation Project of China Academy of Chinese Medical Sciences (CI2026A03401), the Fundamental Research Funds for the Central Public Welfare Research Institutes (ZZ-JQ2023002), and the National Natural Science Foundation of China (82230123).

Institutional Review Board Statement: The animal study protocol was approved by the Ethics Committee of Animal Experiments at the China Academy of Chinese Medical Sciences (approval no. D2024-01-26-07).

Informed Consent Statement: Not applicable.

Data Availability Statement: All data generated or analyzed during this study are included in this published article.

Conflicts of Interest: The authors declare no conflicts of interest.

Abbreviations

The following abbreviations are used in this manuscript:

α7nAChR	alpha-7 nicotinic acetylcholine receptor
AAV	adeno-associated virus
ACh	acetylcholine
AUC	area under the curve

CAP	cholinergic anti-inflammatory pathway
CCK	cholecystokinin
ChAT+	choline acetyltransferase-positive
DMV	dorsal motor nucleus of the vagus
EA	electroacupuncture
ELISA	enzyme-linked immunosorbent assay
ENS	enteric nervous system
FD	functional dyspepsia
GI	gastrointestinal
IA	iodoacetamide
ICCs	interstitial cells of Cajal
OD	optical density
PROKR2	prokineticin receptor 2
ROI	regions of interest
SST	somatostatin
TRPV1	transient receptor potential vanilloid 1
VIP	vasoactive intestinal peptide

References

1. Ford, A.C.; Mahadeva, S.; Carbone, M.F.; Lacy, B.E.; Talley, N.J. Functional dyspepsia. *Lancet* **2020**, *396*, 1689–1702. [CrossRef] [PubMed]
2. Enck, P.; Azpiroz, F.; Boeckxstaens, G.; Elsenbruch, S.; Feinle-Bisset, C.; Holtmann, G.; Lackner, J.M.; Ronkainen, J.; Schemann, M.; Stengel, A.; et al. Functional dyspepsia. *Nat. Rev. Dis. Primers* **2017**, *3*, 17081. [CrossRef] [PubMed]
3. Shin, A. Disorders of gastric motility. *Lancet Gastroenterol. Hepatol.* **2024**, *9*, 1052–1064. [CrossRef] [PubMed]
4. Broeders, B.W.L.C.M.; Carbone, F.; Balsiger, L.M.; Schol, J.; Raymenants, K.; Huang, I.; Verheyden, A.; Vanuytsel, T.; Tack, J. Review article: Functional dyspepsia-a gastric disorder, a duodenal disorder or a combination of both? *Aliment Pharmacol. Ther.* **2023**, *57*, 851–860. [CrossRef] [PubMed]
5. Sayuk, G.S.; Gyawali, C.P. Functional Dyspepsia: Diagnostic and Therapeutic Approaches. *Drugs* **2020**, *80*, 1319–1336. [CrossRef] [PubMed]
6. Cheung, C.K.Y.; Lan, L.L.; Kyaw, M.; Mak, A.D.P.; Chan, A.; Chan, Y.; Wu, J.C.Y. Up-regulation of transient receptor potential vanilloid (TRPV) and down-regulation of brain-derived neurotrophic factor (BDNF) expression in patients with functional dyspepsia (FD). *Neurogastroenterol. Motil.* **2018**, *30*, e13176. [CrossRef] [PubMed]
7. Dong, S.; Zhao, L.; Liu, J.; Sha, X.; Wu, Y.; Liu, W.; Sun, J.; Su, Y.; Zhuang, Z.; Chen, J.; et al. Neuroanatomical organization of electroacupuncture in modulating gastric function in mice and humans. *Neuron* **2025**, *113*, 3243–3259.e11. [CrossRef] [PubMed]
8. Pei, L.; Wang, G.; Yang, S.; Zhou, S.; Xu, T.; Zhou, J.; Zhang, W.; Lu, K.; Hu, L.; Wang, Y.; et al. Electroacupuncture Reduces Duration of Postoperative Ileus After Laparoscopic Gastrectomy for Gastric Cancer: A Multicenter Randomized Trial. *Gastroenterology* **2025**, *169*, 73–84. [CrossRef] [PubMed]
9. Liu, S.; Wang, Z.F.; Su, Y.S.; Ray, R.S.; Jing, X.H.; Wang, Y.Q.; Ma, Q. Somatotopic Organization and Intensity Dependence in Driving Distinct NPY-Expressing Sympathetic Pathways by Electroacupuncture. *Neuron* **2020**, *108*, 436–450.e7. [CrossRef] [PubMed]
10. Liu, S.; Wang, Z.; Su, Y.; Qi, L.; Yang, W.; Fu, M.; Jing, X.; Wang, Y.; Ma, Q. A neuroanatomical basis for electroacupuncture to drive the vagal-adrenal axis. *Nature* **2021**, *598*, 641–645. [CrossRef] [PubMed]
11. Yu, M.; Zhang, L.; Zhang, X.; Wu, A.; Du, S.; Luo, W.; Du, Y.; Li, Q.; Chen, J.; Cao, P. Impaired brain-gut circuit for gut motility dysfunction in mouse models of Parkinson's disease. *Cell Rep.* **2026**, *45*, 117877. [CrossRef] [PubMed]
12. Furness, J.B. The enteric nervous system and neurogastroenterology. *Nat. Rev. Gastroenterol. Hepatol.* **2012**, *9*, 286–294. [CrossRef] [PubMed]
13. Niesler, B.; Kuerten, S.; Demir, I.E.; Schäfer, K.H. Disorders of the enteric nervous system—A holistic view. *Nat. Rev. Gastroenterol. Hepatol.* **2021**, *18*, 393–410. [CrossRef] [PubMed]
14. Furness, J.B. Types of neurons in the enteric nervous system. *J. Auton. Nerv. Syst.* **2000**, *81*, 87–96. [CrossRef] [PubMed]
15. Gao, Y.; Shi, Y.; Wei, M.; Yang, X.; Hao, Y.; Liu, H.; Zhang, Y.; Zhou, L.; Hu, G.; Yang, R. Muscularis macrophages controlled by NLRP3 maintain the homeostasis of excitatory neurons. *Int. J. Biol. Sci.* **2024**, *20*, 476–2490. [CrossRef] [PubMed]
16. Griffiths, J.A.; Yoo, B.B.; Thuy-Boun, P.; Cantu, V.J.; Weldon, K.C.; Challis, C.; Sweredoski, M.J.; Chan, K.Y.; Thron, T.M.; Sharon, G.; et al. Peripheral neuronal activation shapes the microbiome and alters gut physiology. *Cell Rep.* **2024**, *43*, 113953. [CrossRef] [PubMed]
17. Sanders, K.M.; Ward, S.M.; Koh, S.D. Interstitial cells: Regulators of smooth muscle function. *Physiol. Rev.* **2014**, *94*, 859–907. [CrossRef] [PubMed]

18. Sanders, K.M.; Santana, L.F.; Baker, S.A. Interstitial cells of Cajal—Pacemakers of the gastrointestinal tract. *J. Physiol.* **2026**, *604*, 3548–3562. [CrossRef] [PubMed]
19. Wauters, L.; Burns, G.; Ceulemans, M.; Walker, M.M.; Vanuytsel, T.; Keely, S.; Talley, N.J. Duodenal inflammation: An emerging target for functional dyspepsia? *Expert. Opin. Ther. Targets* **2020**, *24*, 511–523. [CrossRef] [PubMed]
20. Deloose, E.; Janssen, P.; Depoortere, I.; Tack, J. The migrating motor complex: Control mechanisms and its role in health and disease. *Nat. Rev. Gastroenterol. Hepatol.* **2012**, *9*, 271–285. [CrossRef] [PubMed]
21. Sanger, G.J.; Furness, J.B. Ghrelin and motilin receptors as drug targets for gastrointestinal disorders. *Nat. Rev. Gastroenterol. Hepatol.* **2016**, *13*, 38–48. [CrossRef] [PubMed]
22. Ferrand, A.; Wang, T.C. Gastrin and cancer: A review. *Cancer Lett.* **2006**, *238*, 15–29. [CrossRef] [PubMed]
23. Zhang, Y.; Tang, Y.W.; Zhou, J.; Wei, Y.R.; Peng, Y.T.; Yan, Z.; Yue, Z.H. Electroacupuncture at ST36 ameliorates gastric dysmotility in rats with diabetic gastroparesis via the nucleus tractus solitarius-vagal axis. *World J. Gastroenterol.* **2025**, *31*, 107395. [CrossRef] [PubMed]
24. Caldarella, M.P.; Azpiroz, F.; Malagelada, J.R. Antro-fundic dysfunctions in functional dyspepsia. *Gastroenterology* **2003**, *124*, 1220–1229. [CrossRef] [PubMed]
25. Choi, Y.J.; Kim, N.; Kim, J.; Lee, D.H.; Park, J.H.; Jung, H.C. Upregulation of Vanilloid Receptor-1 in Functional Dyspepsia With or Without Helicobacter pylori Infection. *Medicine* **2016**, *95*, e3410. [CrossRef] [PubMed]
26. Varghese, C.; Pasricha, P.J.; Abell, T.L.; Parkman, H.P.; Andrews, C.N.; Keszthelyi, D.; Gharibans, A.A.; Farrugia, G.; O'Grady, G. Spectrum of Interstitial Cell of Cajal Deficits in Chronic Gastroduodenal Disorders: Systematic Review and Meta-Analysis. *Am. J. Gastroenterol.* **2026**, *121*, 112–121. [CrossRef] [PubMed]
27. Jiang, L.; Yang, J.; Gao, X.; Huang, J.; Liu, Q.; Fu, L. In vivo imaging of vagal-induced myenteric plexus responses in gastrointestinal tract with an optical window. *Nat. Commun.* **2024**, *15*, 8123. [CrossRef] [PubMed]
28. Myagmarjalbuu, B.; Moon, M.J.; Heo, S.H.; Jeong, S.I.; Park, J.S.; Jun, J.Y.; Jeong, Y.Y.; Kang, H.K. Establishment of a protocol for determining gastrointestinal transit time in mice using barium and radiopaque markers. *Korean J. Radiol.* **2013**, *14*, 45–50. [CrossRef] [PubMed]
29. Jin, M.; Ling, Y.; Jin, L.; Wang, X.; Jiang, X.; Li, Q. Cell membrane-functionalized bismuth oxyiodide nanodots as potential contrast agent for gastrointestinal tract imaging. *Colloids Surf. B Biointerfaces* **2025**, *245*, 114235. [CrossRef] [PubMed]
30. Bendtsen, K.M.; Tougaard, P.; Hansen, A.K. An Early Life Mucosal Insult Temporarily Decreases Acute Oxazolone-Induced Inflammation in Mice. *Inflammation* **2018**, *41*, 1437–1447. [CrossRef] [PubMed]
31. Han, Y.L.; Peng, X.M.; Zhang, H.X.; Chen, S.; Zhang, L.Y. Electroacupuncture Regulates TRPV1 through PAR2/PKC Pathway to Alleviate Visceral Hypersensitivity in FD Rats. *Evid. Based Complement Altern. Med.* **2021**, *2021*, 1975228. [CrossRef] [PubMed]
32. Liu, T.; Ma, M.; Wu, Y.; Asif, I.M.; Chen, D.; Liu, L.; Zhang, M.; Chen, Y.; Li, B.; Wang, L. Protective Effects of Fucoidan on Iodoacetamide-Induced Functional Dyspepsia via Modulation of 5-HT Metabolism and Microbiota. *Int. J. Mol. Sci.* **2025**, *26*, 3273. [CrossRef] [PubMed]
33. Liu, T.; Asif, I.M.; Liu, L.; Zhang, M.; Li, B.; Wang, L. Laminarin ameliorates iodoacetamide-induced functional dyspepsia via modulation of 5-HT3 receptors and the gut microbiota. *Int. J. Biol. Macromol.* **2024**, *268*, 131640. [CrossRef] [PubMed]
34. Wang, Z.; Tang, Q.; Li, K.; Mou, J.; Chen, Y.; Kuang, W.; Sun, L.; Ma, Z.; Wei, Y.; Bao, R.; et al. An enteric-DRG pathway for interoception and visceral pain in mice. *Neuron* **2026**, *114*, 105–121.e6. [CrossRef] [PubMed]
35. Ritsma, L.; Steller, E.J.; Ellenbroek, S.I.; Kranenburg, O.; Borel Rinkes, I.H.; van Rheenen, J. Surgical implantation of an abdominal imaging window for intravital microscopy. *Nat. Protoc.* **2013**, *8*, 583–594. [CrossRef] [PubMed]
36. Pnevmatikakis, E.A.; Giovannucci, A. NoRMCorre: An online algorithm for piecewise rigid motion correction of calcium imaging data. *J. Neurosci. Methods.* **2017**, *291*, 83–94. [CrossRef] [PubMed]
37. Spencer, N.J.; Hu, H. Enteric nervous system: Sensory transduction, neural circuits and gastrointestinal motility. *Nat. Rev. Gastroenterol. Hepatol.* **2020**, *17*, 338–351. [CrossRef] [PubMed]
38. Bonaz, B. Enteric neuropathy and the vagus nerve: Therapeutic implications. *Neurogastroenterol. Motil.* **2025**, *37*, e14842. [CrossRef] [PubMed]
39. Cirillo, C.; Bessissow, T.; Desmet, A.S.; Vanheel, H.; Tack, J.; Vanden Berghe, P. Evidence for neuronal and structural changes in submucous ganglia of patients with functional dyspepsia. *Am. J. Gastroenterol.* **2015**, *110*, 1205–1215. [CrossRef] [PubMed]
40. Rong, P.; Hou, L.; Yang, Y.; Luo, X.; Wang, J.; Zhang, J.; Chen, J.; Wei, W. Multi-targeting regulation of auricular vagus nerve stimulation on gastric hypersensitivity and gastric dysmotility in a rodent model of functional dyspepsia. *Gut Microb. Integr. Wellness* **2023**, *1*, 1–10. [CrossRef]
41. Sato, A. Neural mechanisms of autonomic responses elicited by somatic sensory stimulation. *Neurosci. Behav. Physiol.* **1997**, *27*, 610–621. [CrossRef] [PubMed]

42. Talley, N.J.; Verlinden, M.; Snape, W.; Beker, J.A.; Ducrotte, P.; Dettmer, A.; Brinkhoff, H.; Eaker, E.; Ohning, G.; Miner, P.B.; et al. Failure of a motilin receptor agonist (ABT-229) to relieve the symptoms of functional dyspepsia in patients with and without delayed gastric emptying: A randomized double-blind placebo-controlled trial. *Aliment. Pharmacol. Ther.* **2000**, *14*, 1653–1661. [CrossRef] [PubMed]
43. Gribble, F.M.; Reimann, F. Function and mechanisms of enteroendocrine cells and gut hormones in metabolism. *Nat. Rev. Endocrinol.* **2019**, *15*, 226–237. [CrossRef] [PubMed]
44. Tack, J.; Bisschops, R.; Sarnelli, G. Pathophysiology and treatment of functional dyspepsia. *Gastroenterology* **2004**, *127*, 1239–1255. [CrossRef] [PubMed]
45. Tian, J.H.; Wan, H.Y.; Liu, S.B. Acupuncture effects and neuro-immune regulation: A breakthrough in "treating diseases at the root". *Acupunct. Res.* **2025**, *50*, 538–552. (In Chinese) [CrossRef] [PubMed]
46. Luo, M.; Liu, X.; Qu, Z.; Su, Y.; Jing, X. Approaches to the mechanism research of acupuncture for attenuating inflammatory bowel disease from the perspective of "autonomic nerve-immune" regulation. *Chin. Acupunct. Moxibustion* **2026**, *46*, 631–638. (In Chinese) [CrossRef] [PubMed]
47. Zhao, X.; Chen, T.; Meng, F.; Wang, H.; Tian, P.; Tang, X.; Wang, X.; Wang, X.; Xin, H.; Wei, H. Therapeutic effect of herb residue fermentation supernatant on spleen-deficient mice. *Mol. Med. Rep.* **2018**, *17*, 2764–2770. [CrossRef] [PubMed]
48. Zhang, X.; Hu, X.; Li, J.; Song, X.; Wang, C.; Chen, Y.; Wu, S.; Ma, L.; Jiang, W.; Cai, R.; et al. Electroacupuncture alleviates functional dyspepsia by modulating the vagus nerve to regulate duodenal microbiota and suppress TWEAK/Fn14/NF-κB and arachidonic acid metabolic pathways. *Front. Immunol.* **2026**, *17*, 1746351. [CrossRef] [PubMed]
49. Liang, X.; Yang, J.; Yang, J.; Wang, X.; Yang, Y. Transcriptomic Insights into Biomechanical Modulation of Gastrointestinal Function in A Rat Model of Functional Dyspepsia. *Iran. J. Biotechnol.* **2025**, *23*, e4109. [CrossRef] [PubMed]
50. Leites, M.; Olano, C.; Freire, T. Plasma Interleukin-13 Levels Correlate With the Severity of Symptoms Induced by Functional Dyspepsia. *J. Clin. Gastroenterol.* **2024**, *58*, 865–874. [CrossRef] [PubMed]
51. Mawe, G.M.; Strong, D.S.; Sharkey, K.A. Plasticity of enteric nerve functions in the inflamed and postinflamed gut. *Neurogastroenterol. Motil.* **2009**, *21*, 481–491. [CrossRef] [PubMed]
52. Ge, D.; Zhan, Y.; Wen, Y.; Wu, R.; Xu, Q.; Ao, Z.; Shu, Y.; Tang, X. Microbiota-immune-enteric nervous system interactions in functional constipation: A narrative review and hypothesis-generating framework. *Front. Immunol.* **2026**, *17*, 1851825. [CrossRef] [PubMed]
53. Ma, Q. Somatotopic organization of autonomic reflexes by acupuncture. *Curr. Opin. Neurobiol.* **2022**, *76*, 102602. [CrossRef] [PubMed]
54. Wang, M.; Liu, W.; Ge, J.; Liu, S. The immunomodulatory mechanisms for acupuncture practice. *Front. Immunol.* **2023**, *14*, 1147718. [CrossRef] [PubMed]
55. Rosas-Ballina, M.; Olofsson, P.S.; Ochani, M.; Valdés-Ferrer, S.I.; Levine, Y.A.; Reardon, C.; Tusche, M.W.; Pavlov, V.A.; Andersson, U.; Chavan, S.; et al. Acetylcholine-synthesizing T cells relay neural signals in a vagus nerve circuit. *Science* **2011**, *334*, 98–101. [CrossRef] [PubMed]
56. Carnevale, D.; Perrotta, M.; Pallante, F.; Fardella, V.; Iacobucci, R.; Fardella, S.; Carnevale, L.; Carnevale, R.; De Lucia, M.; Cifelli, G.; et al. A cholinergic-sympathetic pathway primes immunity in hypertension and mediates brain-to-spleen communication. *Nat. Commun.* **2016**, *7*, 13035. [CrossRef] [PubMed]
57. Pavlov, V.A.; Tracey, K.J. The vagus nerve and the inflammatory reflex–linking immunity and metabolism. *Nat. Rev. Endocrinol.* **2012**, *8*, 743–754. [CrossRef] [PubMed]
58. Oh, J.E.; Kim, S.N. Anti-Inflammatory Effects of Acupuncture at ST36 Point: A Literature Review in Animal Studies. *Front. Immunol.* **2022**, *12*, 813748. [CrossRef] [PubMed]
59. Zheng, W.; Song, H.; Luo, Z.; Wu, H.; Chen, L.; Wang, Y.; Cui, H.; Zhang, Y.; Wang, B.; Li, W.; et al. Acetylcholine ameliorates colitis by promoting IL-10 secretion of monocytic myeloid-derived suppressor cells through the nAChR/ERK pathway. *Proc. Natl. Acad. Sci. USA* **2021**, *118*, e2017762118. [CrossRef] [PubMed]
60. Choi, E.L.; Taheri, N.; Tan, E.; Matsumoto, K.; Hayashi, Y. The Crucial Role of the Interstitial Cells of Cajal in Neurointestinal Diseases. *Biomolecules* **2023**, *13*, 1358. [CrossRef] [PubMed]
61. Foong, D.; Zhou, J.; Zarrouk, A.; Ho, V.; O'Connor, M.D. Understanding the Biology of Human Interstitial Cells of Cajal in Gastrointestinal Motility. *Int. J. Mol. Sci.* **2020**, *21*, 4540. [CrossRef] [PubMed]

Disclaimer/Publisher's Note: The statements, opinions and data contained in all publications are solely those of the individual author(s) and contributor(s) and not of MDPI and/or the editor(s). MDPI and/or the editor(s) disclaim responsibility for any injury to people or property resulting from any ideas, methods, instructions or products referred to in the content.